MRI-based motion correction of thoracic PET: initial comparison of acquisition protocols and correction strategies suitable for simultaneous PET/MRI systems

Nikolaos Dikaios,
Wolfson Brain Imaging Centre, Department of Clinical Neurosciences, University of Cambridge, Addenbrooke's Hospital, Cambridge CB2 0QQ, UK

David Izquierdo-Garcia,
Imaging Science Laboratories, Translational and Molecular Imaging Institute, Department of Radiology, Mount Sinai School of Medicine, New York, NY, USA

Martin J. Graves,
Department of Radiology, University of Cambridge, Cambridge, UK

Venkatesh Mani,
Imaging Science Laboratories, Translational and Molecular Imaging Institute, Department of Radiology, Mount Sinai School of Medicine, New York, NY, USA

Zahi A. Fayad, and
Imaging Science Laboratories, Translational and Molecular Imaging Institute, Department of Radiology, Mount Sinai School of Medicine, New York, NY, USA

Tim D. Fryer
Wolfson Brain Imaging Centre, Department of Clinical Neurosciences, University of Cambridge, Addenbrooke's Hospital, Cambridge CB2 0QQ, UK

Abstract

Objectives—Magnetic resonance imaging (MRI) acquired on equipment capable of simultaneous MRI and positron emission tomography (PET) could potentially provide the gold standard method for motion correction of PET. To assess the latter, in this study we compared fast 2D and 3D MRI of the torso and used deformation parameters from real MRI data to correct simulated PET data for respiratory motion.

Methods—PET sinogram data were simulated using SimSET from a 4D pseudo-PET image series created by segmenting MR images acquired over a respiratory cycle. Motion-corrected PET images were produced using post-reconstruction registration (PRR) and motion-compensated image reconstruction (MCIR).

Results—MRI-based motion correction improved PET image quality at the lung-liver and lung-spleen boundaries and in the heart but little improvement was obtained where MRI contrast was

low. The root mean square error in SUV units per voxel compared to a motion-free image was reduced from 0.0271 (no motion correction) to 0.0264 (PRR) and 0.0250 (MCIR).

Conclusions—Motion correction using MRI can improve thoracic PET images but there are limitations due to the quality of fast MRI.

Keywords

Computer simulation; Magnetic resonance imaging; Positron emission tomography; Respiratory-gated imaging techniques; Whole body imaging

Introduction

Respiratory motion during positron emission tomography (PET) leads to a loss of image resolution, degrading detectability and quantification in small structures, such as lung lesions [1]. A number of methods have been developed to correct for this non-rigid motion.

The two major motion correction methods are post-reconstruction registration (PRR) [2] and motion-compensated image reconstruction (MCIR) [3–6]. With PRR each gated acquisition is reconstructed separately, then all the images are registered to the reference gate to form an average motion-corrected image. MCIR embeds the motion model into the iterative reconstruction algorithm to directly produce a single motion-compensated image. Both methods require accurate motion parameters and gating of the data.

The motion parameters can be determined from the PET data itself [2]. However, noise is a problem and not all radiotracers provide the same degree of anatomical information as [^{18}F]fluoro-deoxyglucose (FDG). An alternative approach for PET/CT is to extract the motion parameters from 4D x-ray computed tomography (CT) [3]. However, the sequential nature of PET/CT data acquisition means that the PET and CT data will not be perfectly co-registered, irrespective of the gating method applied. In addition, 4D CT is associated with a high radiation burden [7].

Whole body systems capable of simultaneous PET and magnetic resonance imaging (MRI) are in the prototype phase [8, 9]. One potential advantage of such PET/MRI equipment is the use of MRI information to correct for motion artefacts in simultaneously acquired PET. In fact, combined PET/MRI systems have the potential to provide the gold standard solution for both respiratory motion and any other movement of the patient.

The aim of this study was to provide an initial illustration of the ability of fast MRI sequences to motion correct PET data. Both 3D and 2D MRI acquisitions were examined, with the 2D acquisitions aggregated into 3D images using a novel binning technique. Information obtained from the 3D MRI acquisitions was used to motion correct simulated PET data using both PRR and MCIR.

Materials and methods

4D MRI using 3D acquisition

Following ethical approval, a normal volunteer underwent whole body MRI (Philips 3T Achieva, Philips Healthcare Systems, Best, The Netherlands) at Mount Sinai Medical Centre, New York. 3D images with a 400 mm cubical field-of-view (FOV) and a voxel size of 1.79×8.00×1.79 mm were acquired in coronal planes using a T1-weighted sequence (THRIVE) (TR=1.96 ms, TE=0.82 ms, flip angle of 10°, turbo field echo factor of 72) and a 32 channel cardiac coil. Thirty sequential volumes using a 32% keyhole size [10] and a parallel imaging acceleration (SENSE) factor of 1.5 were obtained with a temporal resolution of 0.64 s.

4D MRI using 2D acquisition

Following ethical approval, another normal volunteer underwent whole body MRI (GE 1.5T HDx, GE Healthcare, Waukesha, WI) at Addenbrooke's Hospital, Cambridge, UK. 2D coronal images with a 474×474 mm FOVand an isotropic voxel size of 3.7 mm were acquired using a balanced steady-state free precession (FIESTA) sequence (TR=5.81 ms, TE= 4.20 ms, flip angle of 70°), an 8 channel cardiac coil and a parallel imaging acceleration (ASSET) factor of 2 resulting in a temporal resolution of 0.40s. Fifteen temporally contiguous images were acquired per plane before moving on to the next plane, with 66 planes acquired covering an anterior-posterior range of 244 mm.

In order to determine 3D motion parameters from the 2D MR images, the latter need to be binned into a 4D image sequence. We propose a new binning technique where image similarity metrics are employed to bin the 2D images. Image-based sorting of 2D images acquired throughout respiration into a 4D image set has previously been applied for CT [11, 12], where it was shown to outperform binning using external respiratory monitoring with the Varian Real-time Position Management (RPM) device (Varian Medical Systems, Palo Alto, CA) [12]. In our approach, initially a 2D image from the first temporal acquisition is chosen. The next 2D image is selected from all the temporal acquisitions of the adjacent coronal plane, according to its correspondence to the initial 2D image (Fig. 1). More specifically, we choose the image that maximizes the normalised mutual information (NMI) [13]; NMI outperformed other metrics (sum of squared differences and correlation coefficient) because of intensity differences between the 2D images. When the 2nd image is chosen, the 3rd image is selected according to its correspondence with the 2nd image. The process continues until all the planes have been processed and then the scheme is repeated for the other temporal acquisitions. Figure 2 compares a 3D volume (gate 6) produced using the proposed scheme to one purely based on acquisition order (i.e., the 6th acquisition for each 2D plane).

Simulated PET data

Eight temporally contiguous MR images from the 3D acquisition were resized to 3.13×3.13×4.25 mm voxels using cubic spline interpolation, cropped in the axial direction to match the PET FOV (153 mm), manually segmented and attributed typical organ FDG standardized uptake values (SUV) to create a corresponding set of pseudo-PET images (Fig.

3). The organs segmented and their SUV values were: lung (0.7), left ventricular myocardium (1.75), liver (2.8), and spleen (2.45). The rest of the body was assigned an SUV value of 0.88. These SUV values were determined from n=3 clinical whole body oncology FDG PET/CT studies, with patients fasted for at least 6 h prior to data acquisition. The pseudo-PET images were then smoothed (6 mm FWHM Gaussian) to simulate realistic PET resolution for the GE Advance; 6 mm is an isotropic approximation to the axial, radial and tangential resolutions measured 10 cm off-axis by Lewellen et al. [14]. To simulate photon attenuation, attenuation images were generated by segmenting the MR images into two classes: lung and soft tissue. The linear attenuation coefficient attributed to lung and soft tissue was 0.036 cm^{-1} and 0.095 cm^{-1} respectively [15]. The SimSET Monte Carlo package (http://depts.washington.edu/simset/html/simset_main.html) was used to model the GE Advance PET geometry (which is also the geometry of the GE Discovery LS PET/CT) and produce attenuated sinogram data for each gate. The total data for all gates gave organ signal-to-noise ratios comparable to those found for a typical 4-minute data acquisition on the GE 690 PET/CT.

Determination of deformation fields

The MR images used to create the pseudo-PET images were registered using a combined affine and non-rigid B-splines algorithm, with mutual information used as the cost function in a multi-resolution approach [6]. Seven deformation fields and their corresponding inverse fields were determined. The motion gate used as the reference (target) corresponded to the mid-point of the respiratory cycle to minimize the average motion between the reference gate and the other gates. In addition, deformation fields were also determined from the noise-free pseudo-PET images using the same registration method as described above for the MR images (Fig. 4).

Generation of motion-corrected images

For PRR the images were reconstructed with an ordered-subsets expectation maximization (OSEM) algorithm [16] implemented in the STIR package [17]. MCIR images were reconstructed by extending the OSEM algorithm in STIR to incorporate motion compensation [6]. For all reconstructions 12 subsets and 20 full iterations were used and the image dimensions were 128×128×35, with a voxel size of 3.13×3.13×4.25 mm. All images were post-filtered with a 6 mm FWHM Gaussian.

Results

Figure 5 and Table 1 show that both PRR and MCIR with deformation fields derived from the 3D MR images produced images (using all gates) more in agreement with the target gate than that produced without motion correction (noMC). Overall, the MCIR image is seen to be superior to that produced by the PRR approach; MCIR has a fundamental advantage over PRR in terms of resolution loss from interpolation applied in the deformation process [6]. Further improvement was found if deformation fields from noise-free pseudo-PET images were used rather than those from the MR images; the superior motion correction in the lateral and medial walls of the spleen and the superior-lateral wall of the liver (coronal plane of Fig. 5) is seen to map to major differences in the deformation fields (Fig. 4).

The improvement over noMC offered by PRR and MCIR with MRI-based deformation fields is further illustrated by the line profiles given in Figs. 6 and 7. The sum of absolute SUV differences between the target and noMC, PRR and MCIR respectively along the axial profiles were: 0.88, 0.72 and 0.57 for lung-liver; 1.14, 0.99 and 0.98 for the myocardium; and 0.94, 0.68 and 0.65 for lung-spleen. The corresponding numbers for the transverse profiles were: 2.35, 1.48 and 1.48 for lung-liver; 1.41, 1.22 and 1.05 for the myocardium; and 1.89, 1.80 and 1.78 for lung-spleen.

Discussion

The ability to acquire anatomical images simultaneously with PET means that whole body PET/MRI systems have the potential to become the new gold standard for motion correction of PET. Although the MRI information could be used to correct motion in all parts of the body, a key region of interest is the torso due to the high degree of non-rigid motion during respiration affecting organs of interest, such as the lung and liver.

In order to adequately sample the respiratory motion, rapid MRI acquisitions are required. The obvious solution is to acquire fast 3D MR images but even with state-of-the art capabilities, such as multi-channel coils, 4D pulse sequences and parallel reconstruction algorithms, there is a compromise in image quality compared to longer acquisitions. In the 3D acquisition used here, in order to obtain the desired temporal resolution the contrast between soft tissues was reduced, which resulted in a loss of registration accuracy and hence errors in the resultant deformation fields. This is illustrated in Fig. 5 where MRI-based motion correction produced little improvement along the lateral boundary of the spleen, whereas deformation fields determined from noise-free pseudo-PET data (which had high contrast in SUV value at this boundary) provided accurate motion correction. However, there was high contrast in the MRI at the lung boundary (Fig. 3) and improvements in PET image quality were found at the lung-liver and lung-spleen interfaces (Figs. 5, 6 and 7).

Due to the reduced contrast and spatial resolution (orthogonal to the coronal plane) of the fast 3D MRI acquisition, we also investigated binning 2D MRI acquisitions into volumes using a scheme based on image similarity metrics. This method was able to produce volumetric MR images with good organ definition (Fig. 2).

An issue for lengthy PET data acquisitions could be the amount of MRI data acquired to monitor motion. One option may be to use 2D MR images in combination with volumetric MRI. Typically the highest degree of respiratory motion is in the coronal and axial directions, and hence a sagittal plane, perhaps through the centre of the right lung, would be best at monitoring this motion. These sagittal 2D acquisitions could also be combined with 2D acquisitions in a central coronal plane to provide information on any rigid-body motion of the patient. Information obtained from 2D MRI acquired throughout the PET data acquisition could be used to provide rigid-body correction and assign the simultaneously acquired PET data to the best matching 3D MRI within a 4D MRI set taken over a number of respiratory cycles. This would not be as accurate as acquiring volumetric MRI throughout the PET data acquisition but it would be a more practical solution; determining deformation fields for volumetric MRI acquired for the entire duration of PET (especially for lengthy

data acquisitions designed for kinetic analysis) would be very computationally expensive. However, irrespective of whether 2D or 3D MRI acquisitions are conducted throughout PET data acquisition, the above approach prevents the acquisition of diagnostic MRI during PET. If diagnostic MRI is acquired before or after PET data acquisition, patient throughput will be reduced and the co-registration of PET and MRI data will be compromised. If it is essential that diagnostic MRI be acquired simultaneously with PET, either the diagnostic MRI will need to have sufficient temporal resolution to allow accurate determina tion of motion parameters or motion correction strategies will have to be developed that combine MRI-based monitoring of motion during part of the PET data acquisition with continuous monitoring throughout PET with an external device such as a respiratory belt or the aforementioned RPM device.

In conclusion, to obtain an indication of the motion correction capabilities of forthcoming whole body PET/ MRI systems, this pilot study examined the quality of motion parameters determined from fast clinical MR images of the torso. Deformation fields from fast 3D MRI improved PET images at the lung-liver and lung-spleen boundaries, and also in the heart, especially for motion-compensated image reconstruction (MCIR) but motion correction was limited in some areas due to low MR contrast. It is proposed that the ultimate motion correction protocol used for PET/MRI may involve a combination of 3D and 2D MRI acquisitions.

Acknowledgments

References

1. Nehmeh SA, Erdi YE, Ling CC, Rosenzweig KE, Schoder H, Larson SM, Macapinlac HA, Squire OD, Humm JL. Effect of respiratory gating on quantifying PET images of lung cancer. J Nucl Med. 2002; 43:876–881. [PubMed: 12097456]

2. Dawood M, Lang N, Jiang X, Schäfers K. Lung motion correction on respiratory gated 3-D PET/CT images. IEEE Trans Med Imaging. 2006; 25:476–485. [PubMed: 16608062]

3. Li T, Thorndyke B, Schreibmann E, Yang Y, Xing L. Model-based image reconstruction for four-dimensional PET. Med Phys. 2006; 33:1288–1298. [PubMed: 16752564]

4. Qiao F, Pan T, Clark JW, Mawlawi OR. A motion-incorporated reconstruction method for gated PET studies. Phys Med Biol. 2006; 51:3769–3783. [PubMed: 16861780]

5. Lamare F, Ledesma Carbayo MJ, Cresson T, Kontaxakis G, Santos A, Cheze Le Rest C, Reader AJ, Visvikis D. List-mode-based reconstruction for respiratory motion correction in PET using non-rigid body transformations. Phys Med Biol. 2007; 52:5187–5204. [PubMed: 17762080]

6. Dikaios N, Fryer TD. Acceleration of motion-compensated PET reconstruction: ordered subsets-gates EM algorithms and a priori reference gate information. Phys Med Biol. 2011; 56:1695–1715. [PubMed: 21346272]

7. van Sörnsen de Koste JR, Senan S, Kleynen CE, Slotman BJ, Lagerwaard FJ. Renal mobility during uncoached quiet respiration: an analysis of 4DCT scans. Int J Radiat Oncol Biol Phys. 2006; 64:799–803. [PubMed: 16298498]

8. Pichler BJ, Kolb A, Nägele T, Schlemmer H-P. PET/MRI: paving the way for the next generation of clinical multimodality imaging applications. J Nucl Med. 2010; 51:333–336. [PubMed: 20150252]

9. Pichler BJ, Judenhofer MS, Wehrl HF. PET/MRI hybrid imaging: devices and initial results. Eur Radiol. 2008; 18:1077–1086. [PubMed: 18357456]

10. van Vaals JJ, Brummer ME, Dixon WT, Tuithof HH, Engels H, Nelson RC, Gerety BM, Chezmar JL, den Boer JA. "Keyhole" method for accelerating imaging of contrast agent uptake. J Magn Reson Imaging. 1993; 3:671–675. [PubMed: 8347963]

11. Pan T, Lee TY, Rietzel E, Chen GT. 4D-CT imaging of a volume influenced by respiratory motion on multi-slice CT. Med Phys. 2004; 31:333–340. [PubMed: 15000619]

12. Zeng R, Fessler JA, Balter JM, Balter PA. Iterative sorting for four-dimensional CT images based on internal anatomy motion. Med Phys. 2008; 35:917–926. [PubMed: 18404928]

13. Studholme C, Hill DLG, Hawkes DJ. An overlap invariant entropy measure of 3D medical image alignment. Pattern Recognition. 1999; 32:71–86.

14. Lewellen TK, Kohlmyer SG, Miyaoka RS, Kaplan MS, Stearns CW, Schubert SF. Investigation of the performance of the General Electric ADVANCE positron emission tomograph in 3D mode. IEEE Trans Nucl Sci. 1996; 43:2199–2206.

15. Madsen MT. PET attenuation correction using mean attenuation coefficients: a simulation study. IEEE Trans Nucl Sci. 1999; 46:2172–2176.

16. Hudson H, Larkin R. Accelerated image reconstruction using ordered subsets of projection data. IEEE Trans Med Imaging. 1994; 13:601–609. [PubMed: 18218538]

17. Thielemans K, Mustafovic S, Tsoumpas C. STIR: software for tomographic image reconstruction release 2. IEEE Nucl Sci Symp Conf Rec. 2006:2174–2176.
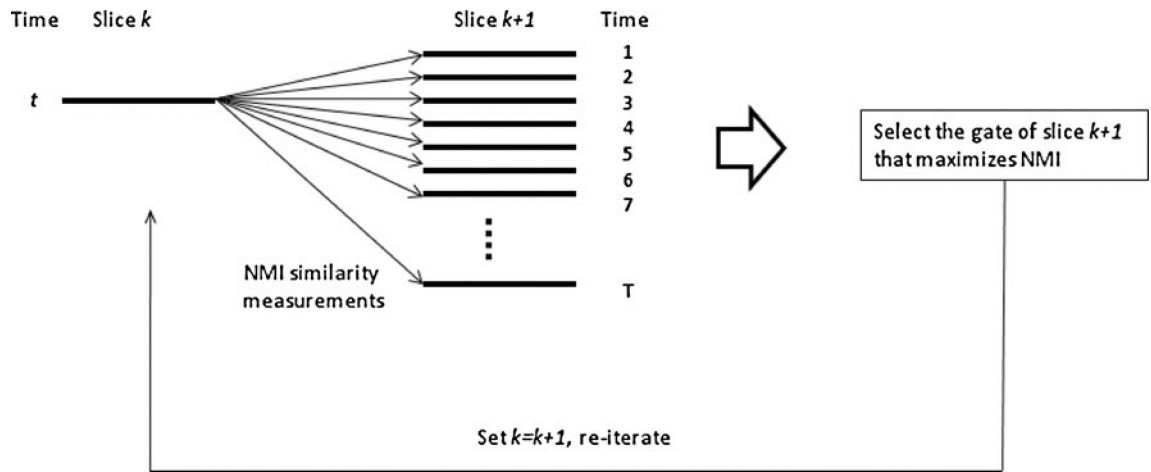
Fig. 1.
Schematic illustration of the binning of 2D MR images into a 3D volume at time *t* based on normalised mutual information (NMI)
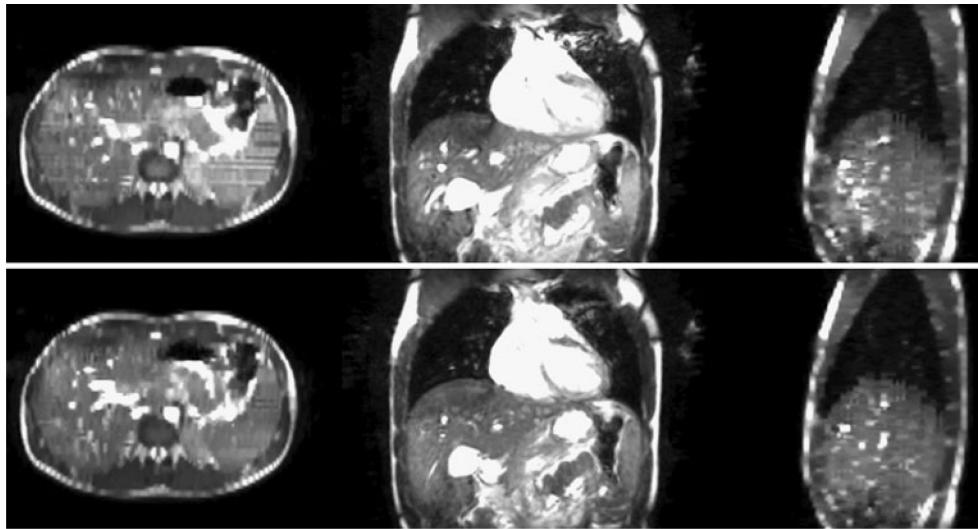
Fig. 2.
Transverse (*left*), coronal (*centre*) and sagittal (*right*) planes for 2D coronal MRI acquisitions aggregated into a 3D volume (respiratory gate 6) based on acquisition order (*top row*) and using normalised mutual information binning (*bottom row*)
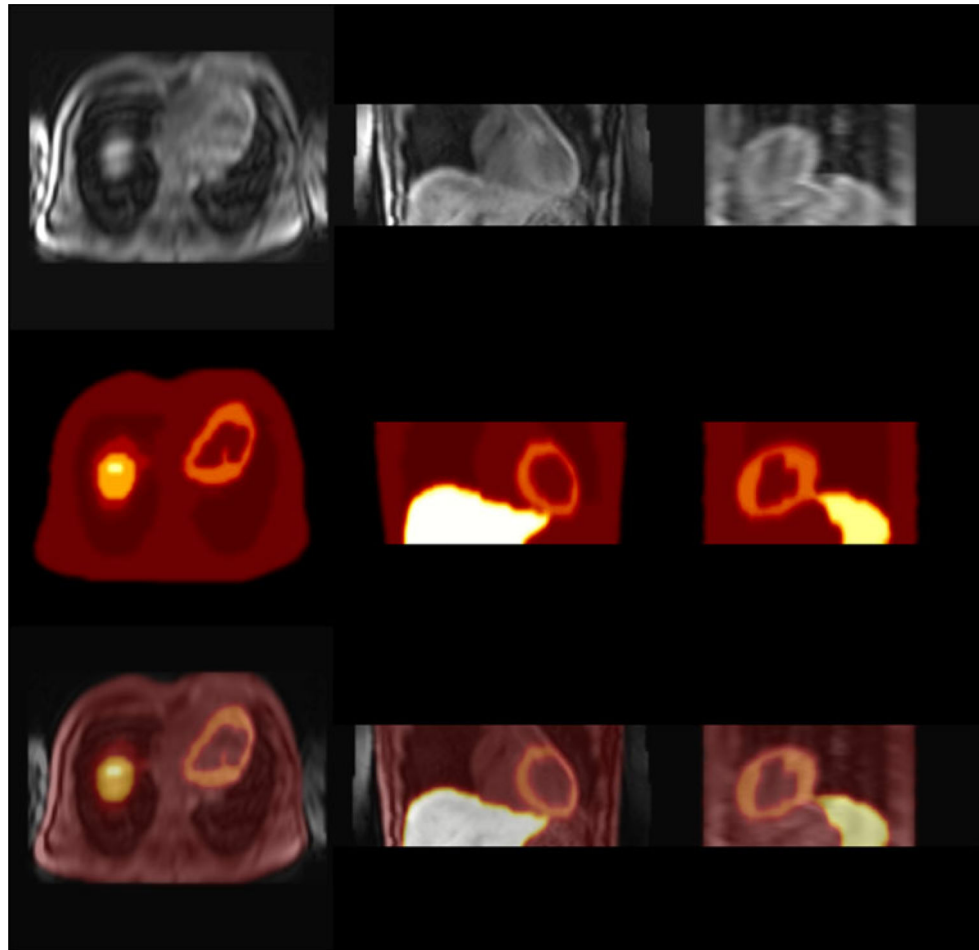
Fig. 3.
Transverse (*left*), coronal (*centre*) and sagittal (*right*) planes through a 3D MRI acquisition (*top row*), the pseudo-FDG image produced by segmenting the 3D MRI (*middle row*) and the fusion of the 3D MRI and pseudo-FDG (*bottom row*). The displayed SUV range of the pseudo-FDG image has an upper threshold of 2.0
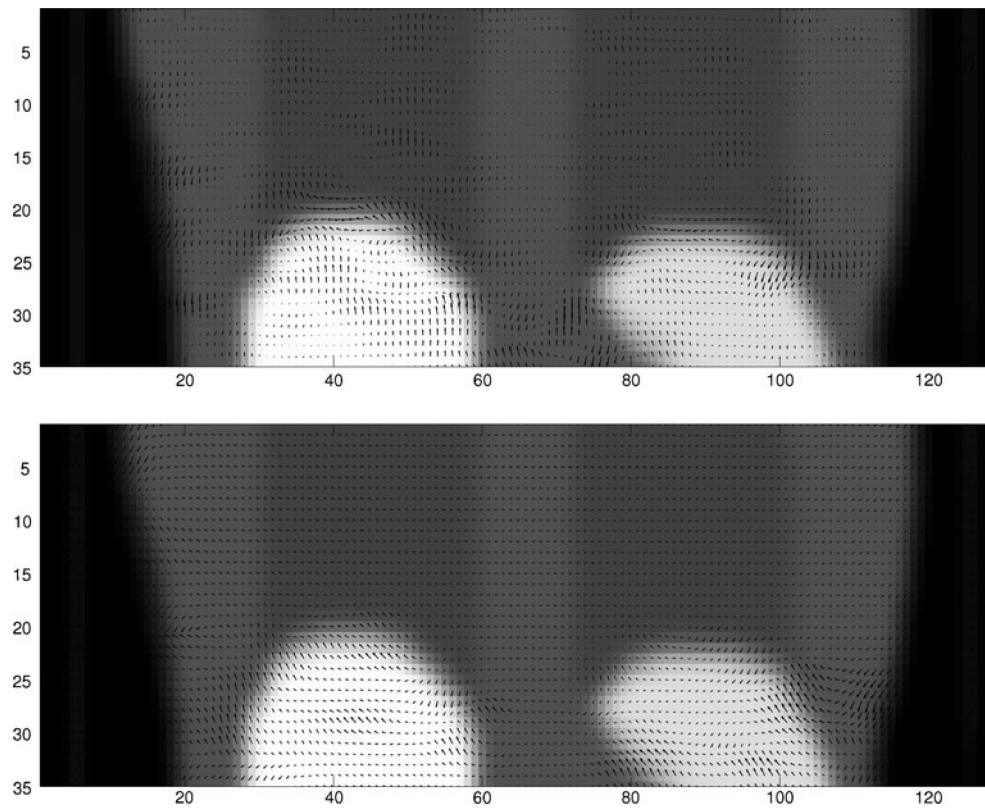
Fig. 4.
Coronal plane of the motion-free target image overlaid with deformation fields determined from MRI (*top*) and the noise-free pseudo-FDG images (*bottom*). The deformation vectors shown are the combination of the *x* (*left-right*) and *z* (*axial*) deformations for registration of gate 1 to gate 3
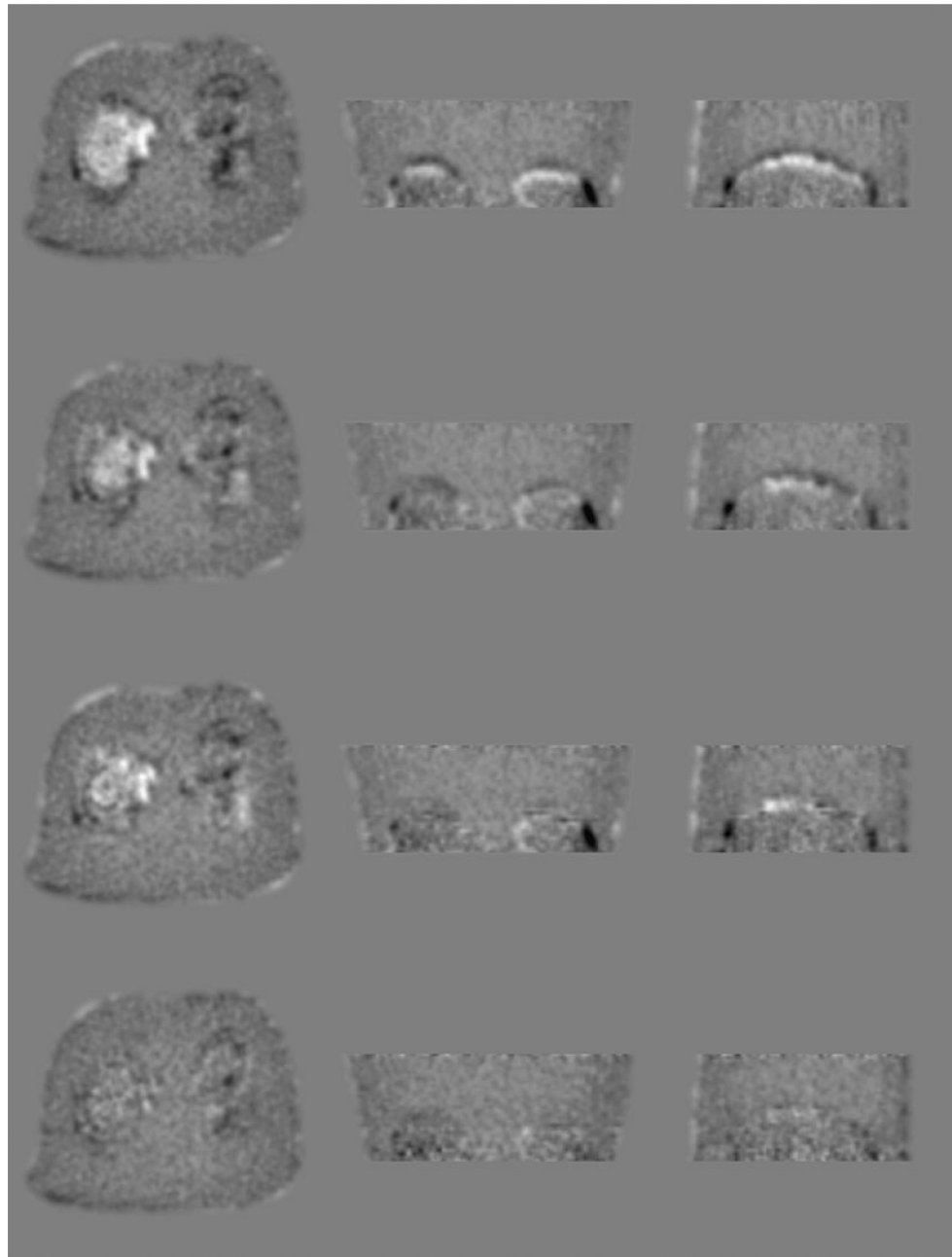
Fig. 5.
Transverse (*left*), coronal (*centre*) and sagittal (*right*) subtraction images between the target image and the following methods: no motion correction (*top row*), post-reconstruction registration with MRI-derived deformation fields (*second row*), and motion-compensated image reconstruction with both MRI-derived deformation fields (*third row*) and deformation fields determined from noise-free pseudo-FDG images (*bottom row*). The SUV range of the images is −0.15 to 0.15. The coronal plane is the same as that in Fig. 4
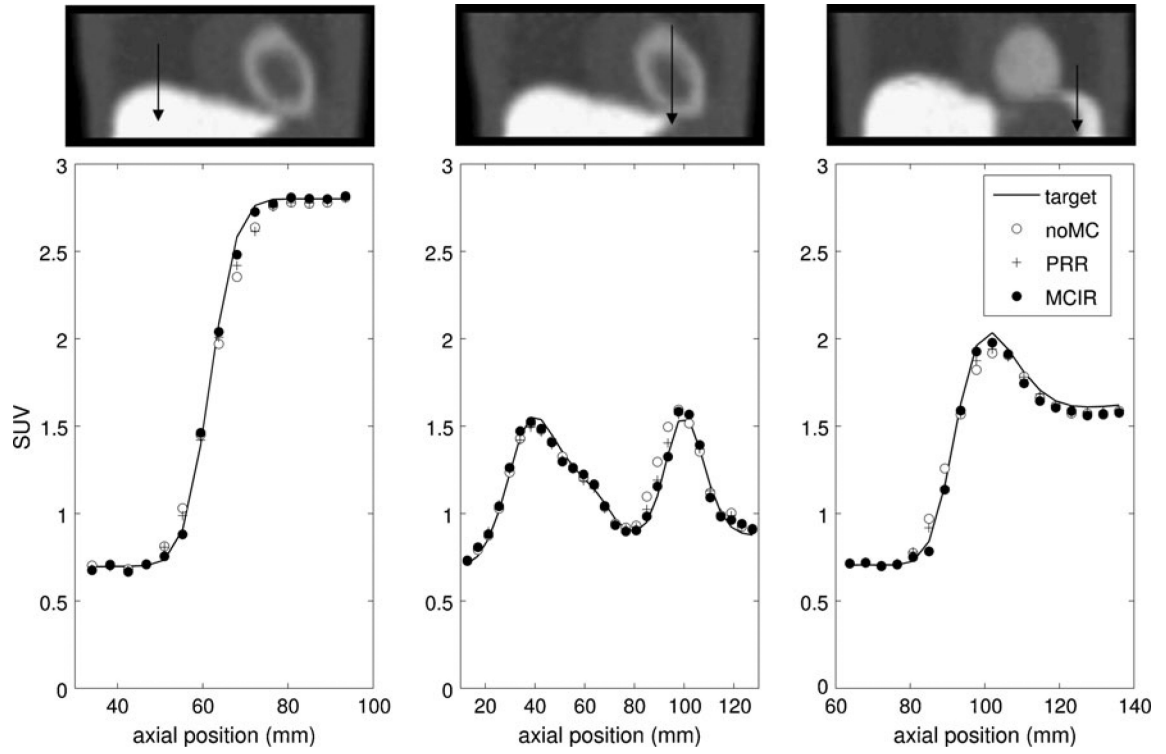
Fig. 6.
Axial line profiles through the lung-liver boundary (*left*), myocardium (*centre*), and lung-spleen boundary (*right*) for no motion correction (noMC), post-reconstruction registration (PRR) and motion-compensated image reconstruction (MCIR) with MRI- derived deformation fields. The solid line denotes the profile through the motion-free target image. Each profile is plotted for the extent of the arrow in the corresponding image. The *arrows* point towards increasing axial position
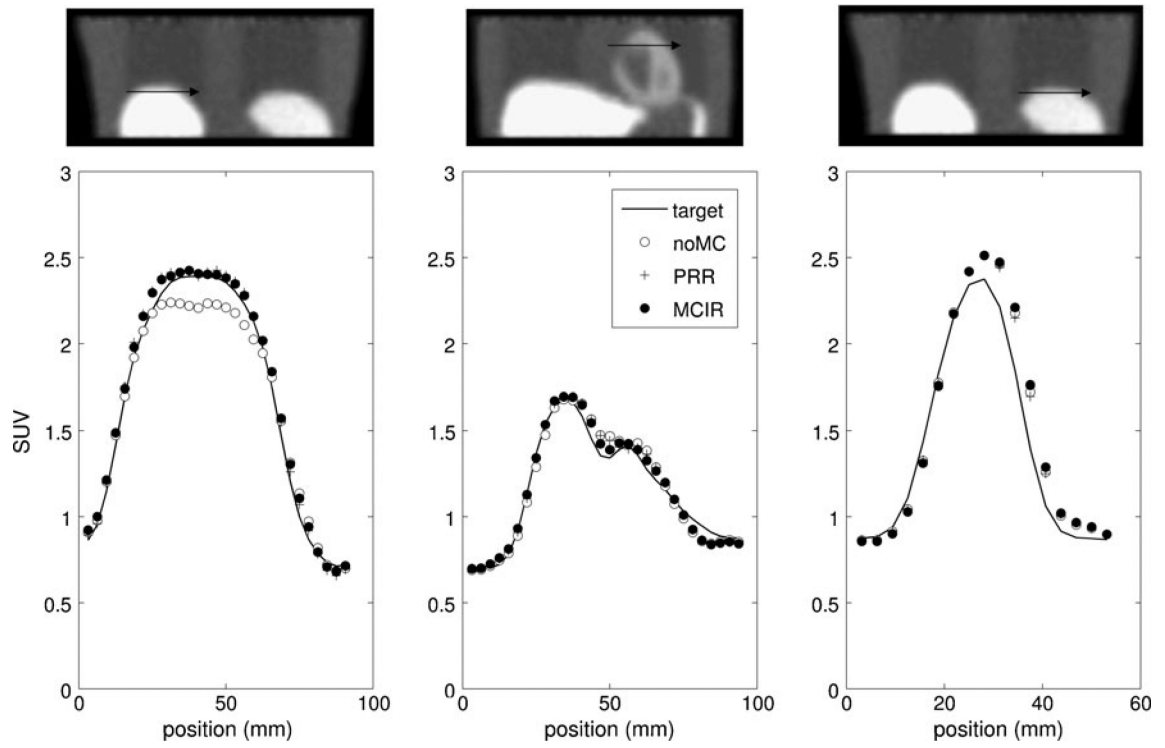
Fig. 7.
Transverse line profiles through the lung-liver boundary (*left*), myocardium (*centre*), and lung-spleen boundary (*right*) for no motion correction (noMC), post-reconstruction registration (PRR) and motion-compensated image reconstruction (MCIR) with MRI-derived deformation fields. The solid line denotes the profile through the motion-free target image

Table 1

Global similarity indices compared to the motion-free target image: root mean square error (RMSE), correlation coefficient (CC), and normalised mutual information (NMI)

	RMSE	CC	NMI
No motion correction	0.0271	0.9982	1.644
PRR (MRI deformation fields)	0.0264	0.9983	1.646
MCIR (MRI deformation fields)	0.0250	0.9985	1.659
MCIR (pseudo-PET deformation fields)	0.0209	0.9991	1.671